Influence of the carbon interface on the mechanical behavior of SiC/SiC composites

C. Fellah, J. Braun, C. Sauder, F. Sirotti, Marie-Hélène Berger

Influence of the carbon interface on the mechanical behavior of SiC/SiC composites

C. Fellah *[a, b], J. Braun [a], C. Sauder [a], F. Sirotti [c, d], M.-H. Berger [b]

[a] *DEN-Service de Recherches Métallurgiques Appliquées, CEA, Université Paris-Saclay, Gif-sur-Yvette F-91191, France*

[b] *MINES ParisTech, PSL Research Université, MAT – Centre des matériaux, CNRS UMR 7633, BP 87-1003 91003 Evry, France*

[c] *Laboratoire de Physique de la Matière Condensée, CNRS, Ecole Polytechnique, IP Paris, 91128 Palaiseau Cedex, France*

[d] *Synchrotron-SOLEIL & Université Paris–Saclay, Saint-Aubin, Boîte Postale 48, F91192 Gif sur Yvette Cedex, France*

* Corresponding author. Clémentine FELLAH, *Laboratoire de Géologie de Lyon : Terre, Planètes, Environnement, Université de Lyon 1, ENS de Lyon, CNRS, UMR 5276, F -69622 Villeurbanne, France*

Tel: +33 4 72 72 84 05. E-mail: clementine.fellah@ens-lyon.fr

Keywords: Ceramic-matrix composites (CMCs), Interface/Interphase, Microstructural analysis

Abstract

SiC/SiC composites reinforced with 3rd generation SiC fibers (Hi-Nicalon S and Tyranno SA3 fibers) are promising candidates for thermomechanical applications in high technology industries. Both composites exhibited a pseudo-ductile mechanical behavior but the HNS/PyC/SiC composite reaches higher failure strains than TSA3/PyC/SiC ones. The mechanical behavior of SiC/SiC composites is linked to the way PyC is bonded to the fiber surface. Analyses have shown that these interactions and the Fiber/Matrix debonding behavior depend strongly on the nature of the carbon on the SiC fiber surface, which is different according to the SiC fiber. In order to understand the mechanism governing the chemical adhesion at the PyC/SiC fiber interface, the formation, the chemistry and the structure of the surface carbon layer were studied. Understanding the origin of this carbon has allowed elucidating the local interaction mechanisms of the studied SiC/SiC composites.

1. Introduction

Ceramic matrix composite materials have aroused interest for aircraft engines as well as for the improvement of the nuclear reactors safety, especially for core materials such as cladding and structural materials [1]–[7]. Among them, SiC fiber-reinforced SiC matrix composites

(SiC/SiC) are promising candidates to replace metallic alloys for these applications. These thermostructural composites have to bear high temperatures and strong mechanical stresses. However, both SiC fibers and SiC matrix are brittle ceramics and their combination in SiC/SiC composites find technological applications only if the composite is damage tolerant and can acquire a pseudo-ductile mechanical behavior [8]–[11].

The ability of SiC/SiC composites to sustain damage is controlled by the fiber/matrix (F/M) coupling mode [12]. The F/M coupling should neither be too strong to prevent matrix cracks propagation through the fibers, nor too weak to allow the load transfer from the matrix to the fibers. In this way, an interphase is deposited on the fibers prior to the matrix infiltration to control this fiber/matrix coupling and provide the damage tolerance of SiC/SiC composites [13]. This layer can be made of pyrolytic carbon (PyC) [14], [15]. The pyrocarbon can provide the suitable bonding strength level to allow load transfer and its structure acts as a fuse regarding the crack propagation. In this way, crack deflection at the SiC/SiC composites interface is favored [16].

Two 3rd generation SiC fibers are chosen for this study, the Hi-Nicalon S (HNS) and the Tyranno SA3 (TSA3) fibers (resp. manufactured by NGS Advanced Fibers and Ube Industries) [17], [18]. From these fibers two composites have been manufactured by CVI (Chemical Vapor Infiltration) using the same process parameters to deposit first a pyrocarbon interphase around the fibers and then the SiC matrix. These SiC/SiC composites have two distinct mechanical behaviors and F/M couplings depending on the nature of their reinforcement [19]. The HNS/PyC/SiC composites exhibit a high damage tolerance, a pseudo-ductile mechanical behavior, resulting from a balanced F/M coupling. On the contrary, the TSA3/PyC/SiC composites have a too strong F/M coupling and are less resistant to mechanical loading that prohibits their use for the aimed applications [20]. However, the TSA3 fibers provide better thermal properties to the composite by their thermal conductivity, justifying the interest in the TSA3-based composites [21].

The distinct F/M coupling strengths of SiC/SiC composites were attributed to differences in the SiC fibers surface characteristics. The intensity of the F/M coupling could be influenced by the fiber surface roughness. The TSA3 fiber surface roughness is three times superior to the HNS fibers one [19]. Matrix cracks generate frictions at the F/M interface with sliding and debonding. A high roughness would cause a strong interfacial sliding resistance [22]. However, previous studies have shown that the SiC fiber surface morphology is not the only key factor controlling the F/M coupling intensity [23]. The interfacial interactions in SiC/SiC composites

between the pyrocarbon and the fiber surface must also be influenced by the microstructure and the chemistry of the SiC fiber surfaces [24]. The local interaction mechanisms are still not well understood. Previous works have identified differences in the structure and chemistry of the carbon rich layer in the first nanometers below the surfaces of the two fibers [19].

Several hypotheses about the origin of the surface carbon have been discussed. This carbon could be formed during the manufacturing of the fibers. The carbon excess in HNS and TSA3 fibers is due to the side methyl groups found in polycarbosilane precursors used for these SiC fibers. Carbon Basic Structural Units (0.7 nm) are observed within a Si-C-(O) amorphous phase at the initial stages of the ceramization [25]. During the crystallisation and growth of SiC grains, the free carbon grows by epitaxy on the SiC grains facets to form turbostratic carbon layers with their (002) planes parallel to the {111} planes of β-SiC grains. This turbostratic carbon is found within the fibers (at the SiC grain boundaries) and also on their extreme surface, i.e. in the near-surface first nanometers, covering SiC surface grains.

The surface carbon could also be formed by the pyrolysis of the sizing polymer, first step of the composites processing. The as received commercial fibers are coated by a thin polymer layer to protect them and ease the textile shaping processes. A thermal treatment is performed to remove the sizing on the fibers before the manufacturing steps of the SiC/SiC composites. However, carbonaceous residues could remain at the fiber surface after this treatment and contribute to the carbon layer rich extreme surface [26].

This work aims to elucidate the local bonding modes governing the F/M coupling and damage mechanisms at the F/M interface of these two composites. Firstly, the thermal decompositions of the sizing polymers have been studied using thermogravimetric analysis and X-Ray Photoelectron Spectroscopy to investigate its contribution to the formation of the carbon rich surfaces on the two SiC fibers. Then the interfacial regions have been characterized using High Resolution Transmission Electronic Microscopy (HRTEM) and their structural modifications after mechanical loading up to failure have been followed. In addition composite without PyC interfaces (SiC/SiC) have been prepared for comparison, analyzed by HRTEM before and after mechanical loading. The understanding of the origin, the role and the formation mechanisms of the carbon on the fiber surface opens up the possibility to design a surface treatment to improve the mechanical behavior of the TSA3-based SiC/SiC composites.

2. Experimental procedures

2.1. Materials

The two nearly stoichiometric commercial fibers, the Hi-Nicalon S (HNS) and Tyranno SA3 (TSA3) have mean diameters of 13 µm and 10 µm, C/Si atomic ratios of 1.02 and 1.08 and low oxygen levels of 0.2 and 0.3% at., respectively. Table 1 summarizes the main characteristics of the two fibers, as given by the manufacturers. These fibers are highly crystalline and the excess carbon forms turbostratic intergranular pockets [27], [28]. The HNS and TSA3 fibers have high Young's moduli (373 and 368 GPa respectively), a tensile strength ranging from 2.24 to 3.01 GPa and a failure strain about 0.7% [19], [24].

The HNS fibers are characterized by a homogeneous chemical composition from the core to the surface except at the extreme surface where a carbon enrichment is observed [29]. On the contrary, the TSA3 fibers contain more free carbon in the core than at the surface (from 16% at. to 4% at., respectively). This gradient originates from the synthesis of the TSA3 fibers derived from a Si-Al-C-O precursor [30], [31]. The chemistry of the TSA3 precursor also induces the presence of about 1000 ppm of aluminum and 3000 ppm of bore in the ceramic fiber [32], [33]. The TSA3 grain size ranges from 200 to 400 nm, whereas the HNS one lays between 10 and 50 nm. The higher surface roughness of TSA3 fibers is directly related to its higher grain size. It also explains its higher thermal conductivity compared to the HNS fibers (65 against 18 $W.m.K^{-1}$ for HNS fibers at 25°C). This makes TSA3 fiber more attractive for thermal applications in extreme thermal conditions [21]. Both SiC fibers are protected by a polymer layer: the poly(vinyl alcohol) (PVA) for HNS fibers and the polyoxyethylene (POE) for TSA3 fibers.

Properties	Hi-Nicalon S (HNS)	Tyranno SA3 (TSA3)
Batch	520226	S1F08PX
Fiber diameter (µm)	13	10
Number of fibers per tow	500	800
Tex ($g/10^3m$)	199	175
Density (g/cm^3)	3.05	3.01
Sizing amount (%wt)	1.13	0.59
Tensile strength (GPa)	3.01	2.24
Tensile modulus (GPa)	373	368
Failure strain (%)	0.81	0.61
Oxygen content (%wt)	0.2	0.3

Table 1. Main characteristics of Hi-Nicalon Type S and Tyranno SA3 fibers

Interlock 2.5D woven fabrics with 0° and 90° fiber orientations were produced. The decomposition of the sizing was obtained after the weaving by thermal treatment of the fibers at 900°C under vacuum for 2h. Then infiltration a pyrocarbon interphase (PyC) and SiC matrix

or only the SiC matrix were achieved by CVI. A final 30 – 40 % fiber volume fraction in the composite was reached. The PyC texture was highly anisotropic to optimize fiber/matrix coupling [34]. This interphase was ~ 50 nm thick (figures 1a. and 1b.). The SiC/SiC composites in this study had a porosity rate between 7.5% and 9%.

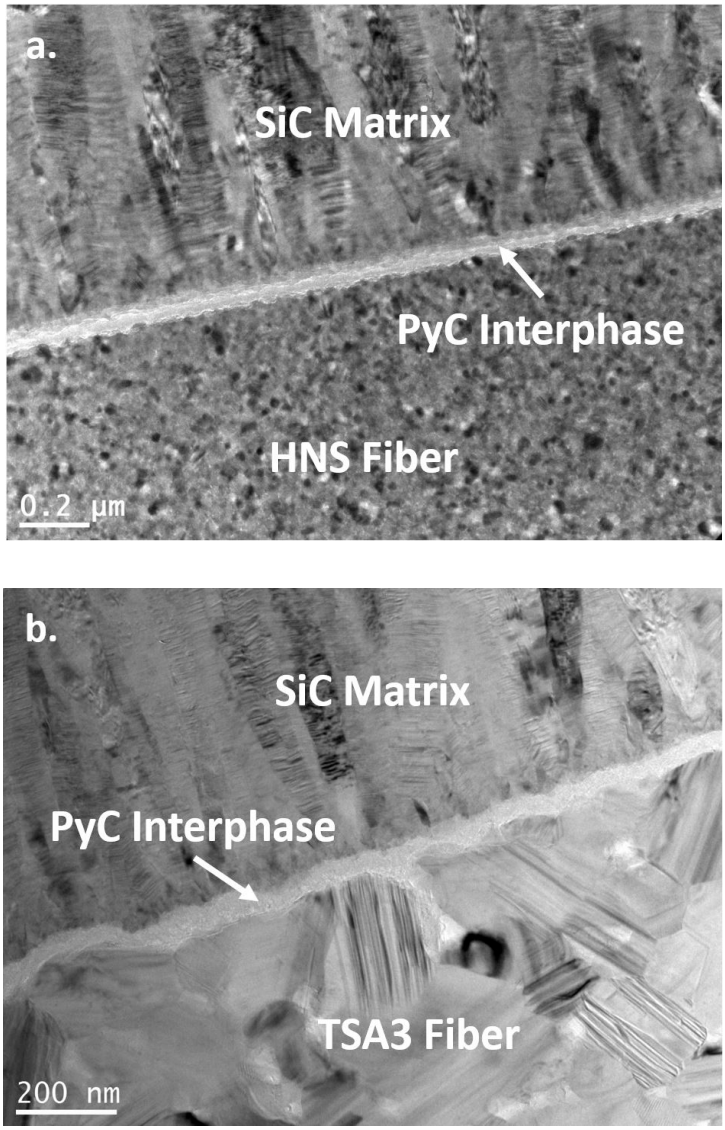

Figure 1. TEM cross-section of the interface of SiC/PyC/SiC composites reinforced by HNS fibers (a.) and TSA3 fibers (b.)

2.2. Thermal analysis

The thermal decomposition of the fiber sizing was followed by a thermogravimetric analyzer (SETSYS- Setaram Evolution Analytical). The experimental parameters for these analyses were close to the desizing ones and were carried out between 10^{-3}-10^{-5} mbar with a thermal ramp of 2.5°C/min up to 900°C followed by a 2 hours' isotherm at this temperature. The sizing

decomposition was also analyzed with a thermal cycle including a 48 h isotherm at 900°C to detect any further weight evolution at longer time scales. The weight changes obtained during thermogravimetric analysis were determined relatively to the theoretical weight of the sizing initially covering the HNS and TSA3 fibers. These tests were repeated five times for each fiber type to ensure the reproducibility of the measurements. Changes in the morphology of the fiber surfaces after these heat treatments were observed by SEM (SEM FEI Nova NanoSEM 450) coupled to an EDS detector at 5 keV.

2.3. Chemical analysis

High Resolution X-Ray Photoemission Spectroscopy was used to study the chemistry and bonding configuration of the HNS and TSA3 fibers surface. These analyses were performed on the TEMPO beamline (Time resolved Experiments on Materials with Photoelectron Spectroscopy) of SOLEIL synchrotron [35]. The synchrotron beam had a diameter of 100 µm for the study and its energy could be tuned at 400, 700 (baseline energy for the experiment) and 1000 eV to probe any changes in chemistry in the near surface region from 2 to 6 nm below the surface. This probing depth is considered to be three times the inelastic mean free path of the photoelectrons [36]. Prior to these analyses, the desized fibers were heat treated at about 900°C within the TEMPO line to get closer to the surface configuration after desizing.

Carbon to silicon ratio was deduced from XPS spectra recorded in the 0-600 eV binding energy range and high-resolution spectra of carbon core level (C_{1s} peak) were recorded and fitted using XPS CASA software. The XPS lineshape was represented by a symmetrical Gaussian-Lorentzian function. The Csp^2 component was fitted by an asymetrical model (Doniach-Sunjic function). A Shirley background substraction was applied for the high-resolution spectra.

2.4. Mechanical tests

Room-temperature tensile tests were carried out on SiC/SiC plates using an Instron 2404 tensile testing machine. Plates were 55 mm length, 8 mm width and 1 mm thick. The gauge length was 25 mm. Aluminium end tabs were glued (3M Scotch-Weld™ 9323 B/A), on both sides of the specimens. A 25 kN load cell was used, crosshead displacement rate was 0.05 mm/min to 0.2 mm/min and specimen elongation was measured with an extensometer fixed onto the plates (Instron 2620-603). The displacement speed was raised during loading-unlodaing tensile tests to limit the duration of tests. There was no influence of displacement rate in this range (0.05 to

0.2mm/min). The fracture surfaces were examined by scanning electron microscopy (SEM FEI Nova NanoSEM 450).

2.5. Microstructural analysis

The SiC fiber extreme surfaces and the interphase regions of SiC/ (PyC/) SiC composites were investigated by Transmission Electron Microscopy (TEM, FEI Tecnai F20 ST operating at 200 kV). Carbon (002) lattice fringe images were recorded to investigate the structural organization of the carbon-rich surfaces on the fibers and the composite interface regions before and after mechanical loading. Thin foils of the surface of the desized SiC fibers were prepared by Focused Ion Beam (MEB-FIB Zeiss Auriga 40) and those of SiC/SiC composites by Ion Slicer (Jeol IS).

After mechanical tests of SiC/SiC composites, many cracks have propagated close to the surface of the fibers. Using the FIB has allowed to extract a region where cracks have propagated between the fiber and the matrix (figure 2). The samples were previously mounted with epoxide resin and polished. The mounting resin has impregnated even within cracks from mechanical tests. The thin foil is extracted from the sample following the lift-out method [37] and thinned down to 100 nm using the gallium ion beam.

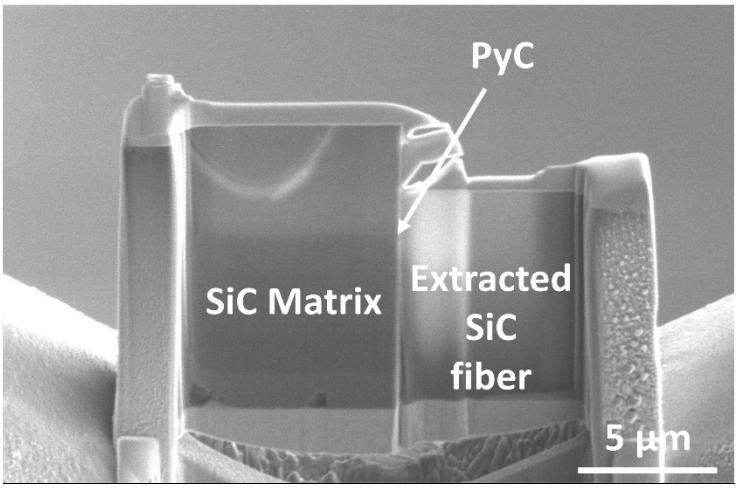

Figure 2. SEM image of FIB thin foil around an extracted fiber in a SiC/SiC composite

3. Results

3.1. Characterization of the fibers surface

3.1.1. Thermal and chemical analysis

The temperature profile and the weight changes of the sized fibers during the thermogravimetric analysis are represented on Figure 3a.

Successive weight losses were identified on the weight change profile of the HNS fibers and could be correlated to the thermal decomposition of their sizing polymer (PVA) [38]–[40]:

- From 150°C to 230°C for a weight loss of 25 %. The first mass loss refers to the dehydration of PVA. Water molecules are removed to lead to the formation of conjugated polyene macromolecules around 200°C [41].
- From 240°C to 450°C for a weight loss of 50 %. The C-C bonds scission of the PVA main chain results in the formation of terminal carbonyls groups between 300°C and 500°C [42].

The final weight loss was equivalent to 55 % of the sizing amount present initially on the HNS fibers (1.13 %wt of HNS fibers). The sizing was not completely decomposed and evaporated on the HNS fibers at 900°C on contrary to the TSA3 fibers. The final weight loss for the TSA3 fibers was 93 % relative to the initial amount of the sizing (0.59 %wt of TSA3 fibers). The decomposition of the TSA3 sizing polymer (POE) occurred in a single step between 290°C and 360°C [43]–[46].

The thermal decompositions of the HNS and TSA3 fiber sizings were followed thereafter with a thermal cycle including an isotherm at 900°C during 48 hours (Figure 3b.). This extended isotherm revealed if the mass loss, obtained at the end of the previous thermogravimetric test, continued to evolve or was stabilized. Based on figure 3b, this thermal cycle applied the HNS fiber sizing did not allow to decrease below 50 % the side products of the sizing and to decompose and evaporate completely the sizing, whereas the POE was well eliminated from the TSA3 fibers.

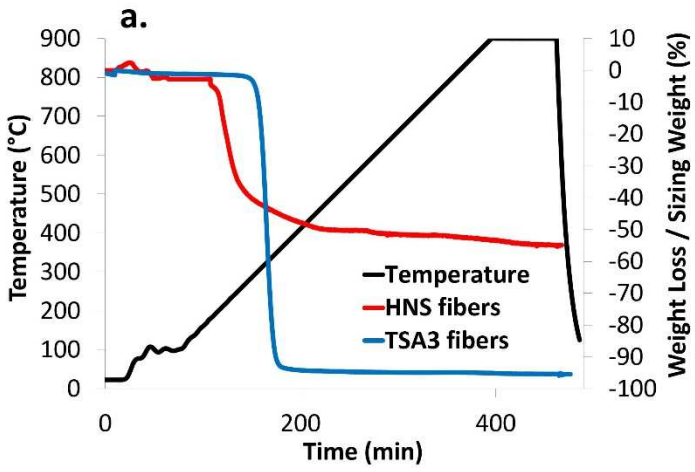

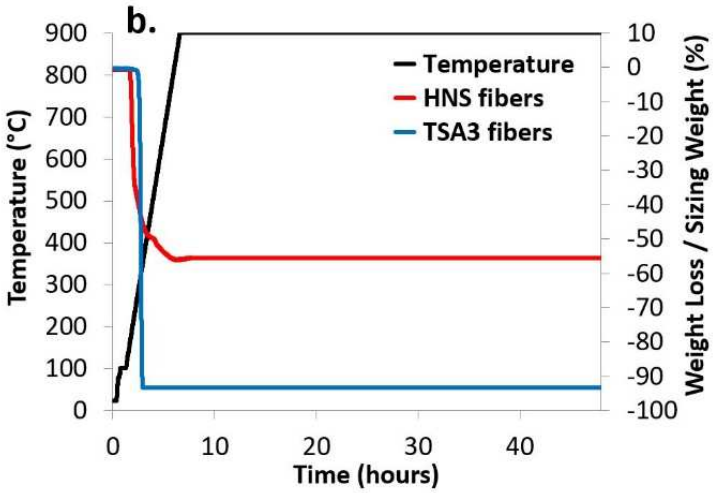

Figure 3. Thermogravimetric analysis of the HNS and TSA3 sized fibers with an isotherm at 900°C during 2 hours (a.) and 48 hours (b.)

The fibers surface chemistries were analysed after desizing. Photoemission spectra obtained at 700 eV are shown in figure 4a. and the evolution of the C/Si ratio according to the beam energy in figure 4b. These analyses indicated that the carbon was the predominant element on the extreme surface of both desized fibers. Oxygen, silicon and calcium were also detected (from O_{1s}, Si_{2p} and Ca_{2p} peaks). Calcium originated from the aqueous bath in which the sizing was added. The surface composition of the HNS fibers was similar from a probed region to another one for a given beam energy. However, the carbon concentration, and so the C/Si, decreased with the probed thickness (i.e. higher incident energy) due to the contribution below the surface of the silicium carbide. The C/Si ratio of the TSA3 fibers surface was lower than the HNS one.

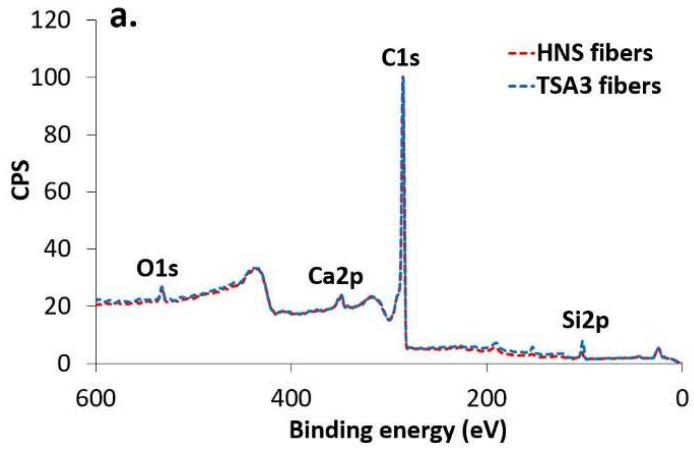

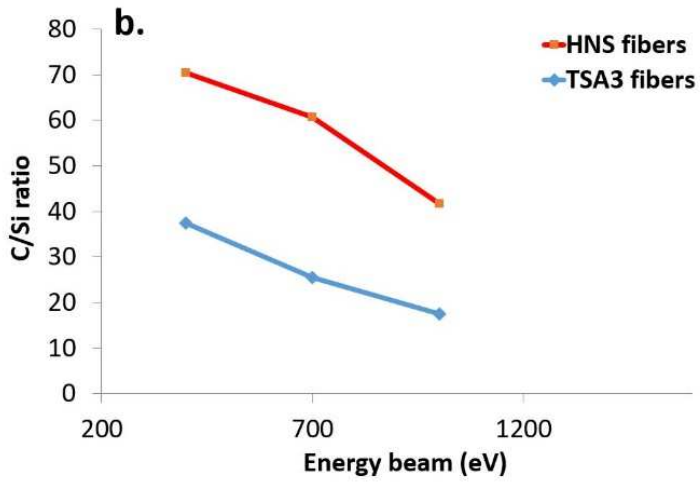

Figure 4. Overview spectra of the surface of the HNS and TSA3 desized fibers at 700 eV (a.) and C/Si ratio of the HNS and TSA3 desized fibers relative to the energy beam (b.)

The C1s peak deconvolution (figure 5) revealed different contribution of carbon bonds (Csp^2, Csp^3, C-O, C-Si, SiC_xO_y) for the HNS and TSA3 fibers as shown in table 2. The sp^2 hybridized C-C was the major C bonding mode for both SiC fiber surfaces. This contribution is even higher for the TSA3 fibers (~ 80 % of C at.) than for the HNS fibers (~ 70 % of C at.), this could be associated with the higher concentration of turbostratic carbon on the TSA3 fiber surface [47]. The fraction of sp^3 hybridized carbon was higher on the HNS fiber surface (19 % of the carbon bonds). This carbon layer was therefore not completely composed of graphitic units and could be closer to the structure of some amorphous carbons [48]–[50].

In the HNS fiber, around 3.5% of near surface carbon was engaged in a silicon oxycarbide phase (SiC_xO_y), whereas silicon carbide (SiC) did not contribute to the extreme surface composition probed. On the contrary, for the TSA3 fiber, the contribution of the Si-C bonds had to be added for the deconvolution of its C_{1s} peak. The Si-C bonds and SiC_xO_y were observed on all scales of depth of these analyses, ranging from 4 to 8 nm. The carbon rich layer on TSA3 fiber surface was thinner than the HNS fiber one and so, SiC grains were closer the extreme fiber surface. The C-O bonds of both SiC fiber surfaces were hydrocarbon pollutants that could be deposited when the fibers are exposed to air [51].

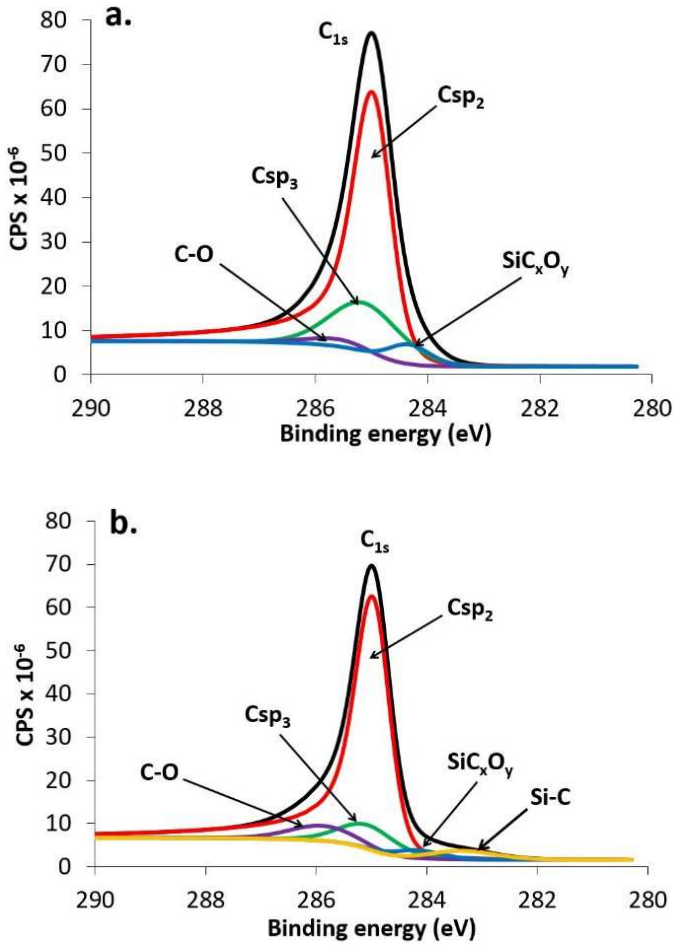

Figure 5. High-resolution spectra of carbon (C_{1s} peak) of the surface of the HNS (a.) and TSA3 (b.) desized fibers at 700 eV

Energy (eV)	Depth (nm)	Fibers	Csp^2 (% at.)	Csp^3 (% at.)	C-O (% at.)	SiC_xO_y (% at.)	SiC (% at.)
400	2	HNS	72.7 (± 2.1)	19.2 (± 0.7)	5.1 (± 1.6)	3.6 (± 1.7)	/
		TSA3	82.8 (± 4.0)	8.2 (± 0.7)	3.8 (± 0.4)	4.5 (± 2.0)	1.0 (± 0.1)
700	4	HNS	71.8 (± 1.5)	19.0 (± 0.7)	5.7 (± 0.6)	3.7 (± 2.6)	/
		TSA3	82.2 (± 1.7)	8.8 (± 0.3)	4.3 (± 0.4)	2.5 (± 0.4)	2.3 (± 1.0)
1000	6	HNS	74.7 (± 0.5)	18.6 (± 0.6)	3.2 (± 1.3)	3.5 (± 0.4)	/
		TSA3	79.2 (± 1.6)	9.3 (± 0.8)	5.4 (± 0.1)	3.0 (± 0.8)	3.4 (± 0.8)

Table 2. C1s peak contributions of HNS and TSA3 desized fibers relative to the energy beam

3.1.2. Microstructural analysis

The desized HNS fibers observed by SEM, exhibited many surface heterogeneities (figure 6a.) that could explain the incomplete weight loss obtained at the end of the previous thermogravimetric analyses and the photoemission results with ~19% of sp^3 carbon bonds. These non-spherical clusters could have dimensions going hundreds of nanometers to one micrometer. EDX analysis at 5 keV made on the largest one revealed mainly carbon. Their

spatial distribution was rather heterogeneous. When observed in TEM (Figure 6b.), and HRTEM (Figure 6c.), these carbon particles exhibited an amorphous structure. An amorphous outer carbon layer, approximately ten nanometers thick, was also noticed (Figure 6d.). The carbon layer and clusters had a similar structural organization responsible for the sp^2/sp^3 carbon detected by photoelectron spectroscopy.

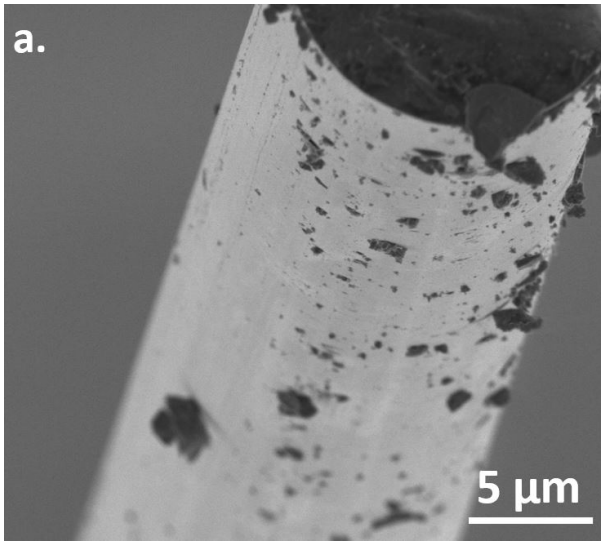

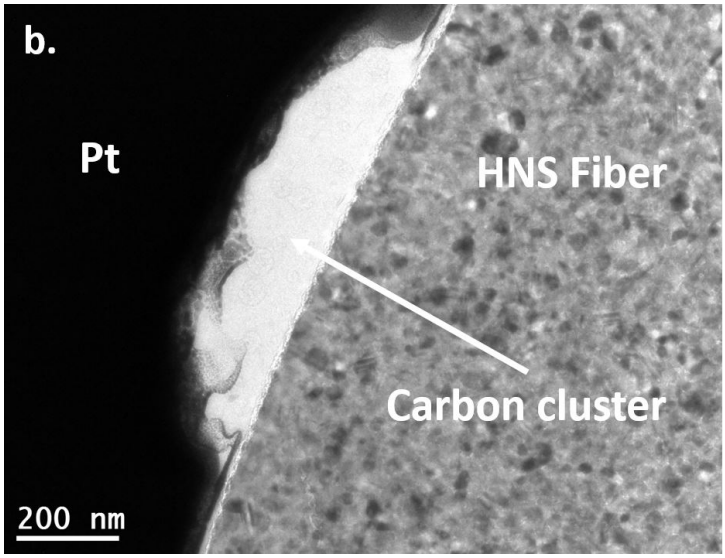

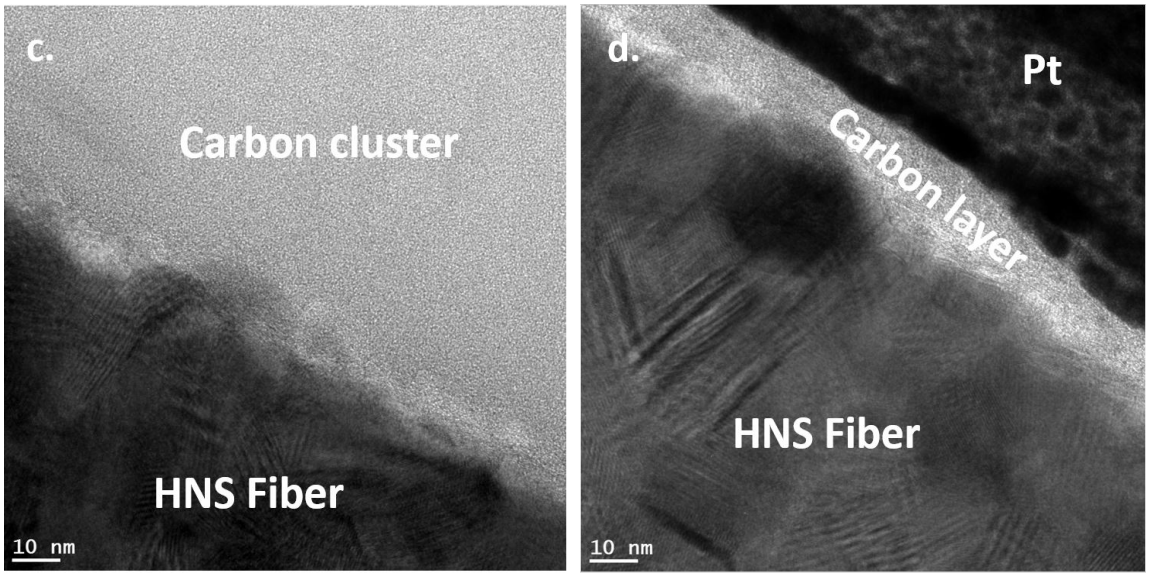

Figure 6. SEM image of a desized HNS fiber (a.), TEM cross-section of the surface of a HNS desized fiber (b.), HRTEM image of the carbon cluster (c.) and the carbon layer (d.) on the surface

The HRTEM of fig 7 shows a few carbon stacks exceeding three graphene layers, located solely on the surface of SiC grains. This carbon originated from the excess carbon of the fiber before its sizing. The carbon attributed to the desizing process showed some stacks of 2 to 3 few graphene sheets associated with a lateral lenght (L_a) not exceeding 0.8 nm. They corresponded to the early stage of carbon organization, described by M. Guigon [52] as basic structural units (BSU) from 8 to 12 Å of lateral length and at least two fringes.

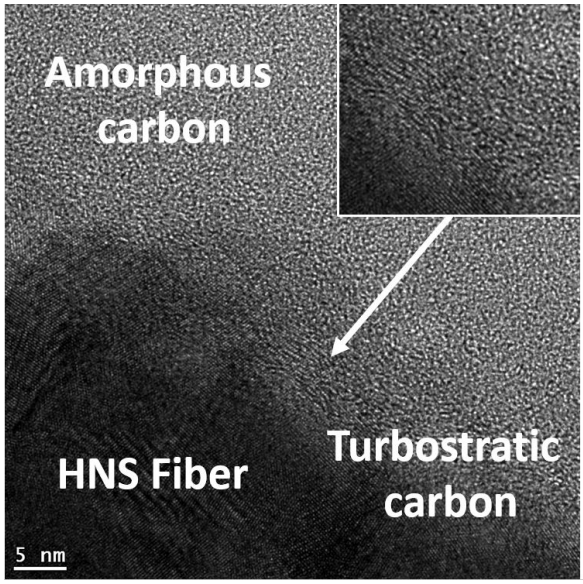

Figure 7. HRTEM image of HNS desized fiber

No clusters of amorphous carbon were observed on the desized TSA3 fiber surface (Figure 8a.). Discontinuous stripes of turbostratic carbon were found on the surface of some SiC grains, made of ~ 10 graphen layers (Figure 8b.). These observations confirm the high sp^2 carbon contribution of C_{1s} peak obtained by high resolution photoemission spectroscopy. The nucleation of the carbon on the TSA3 fiber surface has not occurred on all the SiC grain facets. This explains why the Si-C bonds were highlighted even for the lowest probed depths.

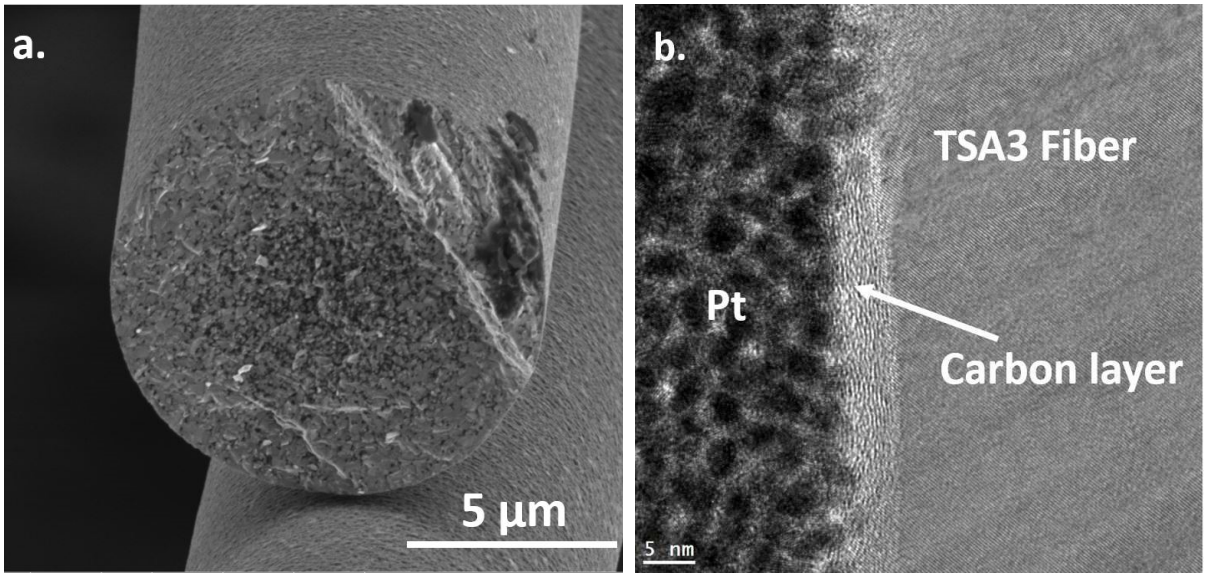

Figure 8. SEM image of TSA3 desized fibers (a.), HRTEM image of the surface of TSA3 desized fiber (b.)

3.2. Microstructural analysis of the F/M interface of SiC/SiC and SiC/PyC/SiC composites

3.2.1. SiC/SiC and SiC/PyC/SiC composites reinforced by HNS fibers

When the desized HNS fiber was incorporated in a SiC matrix without PyC interphase, the two structures of carbon described above for the desized fiber could be recognized at the fiber/matrix interface (figure 9a.): the carbon rich amorphous layer and the turbostratic carbon clusters associated to the free carbon which developped preferentially parallel to the {111} plans of the SiC grains. When a PyC interphase was added on the desized HNS fiber before the matrix infiltration, the interphase was deposited on the amorphous carbon layer previously described. Most of the PyC stacks were parallel to the HNS fiber axis (figure 9b.) except locally for the very first layers deposited close to the amorphous carbon layer.

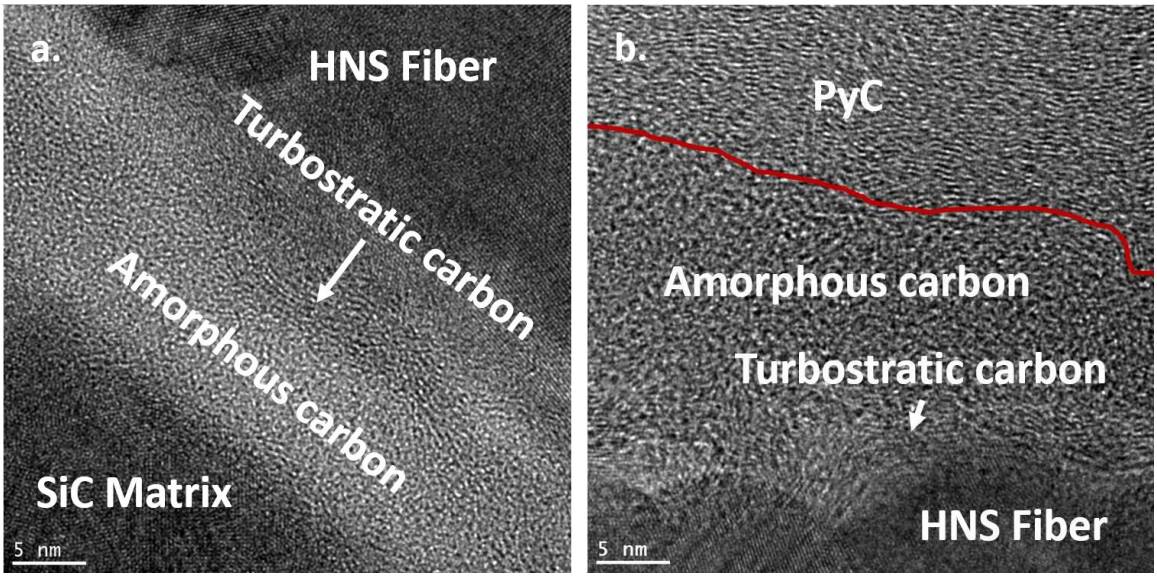

Figure 9. HRTEM images of the F/M interface of the HNS/SiC composite (a.) and of the HNS/PyC/SiC composite (b.)

3.2.2. SiC/SiC and SiC/PyC/SiC composites reinforced by TSA3 fibers

The turbostratic carbon ribbons were always identified on the TSA3 fiber surface of the TSA3/SiC composite, following the {111} facets of the SiC grains (figure 10a.). No amorphous carbon was observed at the F/M interface of TSA3/SiC composite, which confirms its absence on TSA3 fibers surface. The PyC of the TSA3/PyC/SiC composite developped parallel to the fiber surface and in continuity to the turbostratic carbon (figure 10b.). The interface between these two carbons was difficult to determine. The carbon of TSA3 fibers surface is used as a seed for the PyC growth. The microstructural organization of the PyC interphase in TSA3/PyC/SiC composite is higher than the one of the PyC deposited on HNS fiber in HNS/PyC/SiC composite.

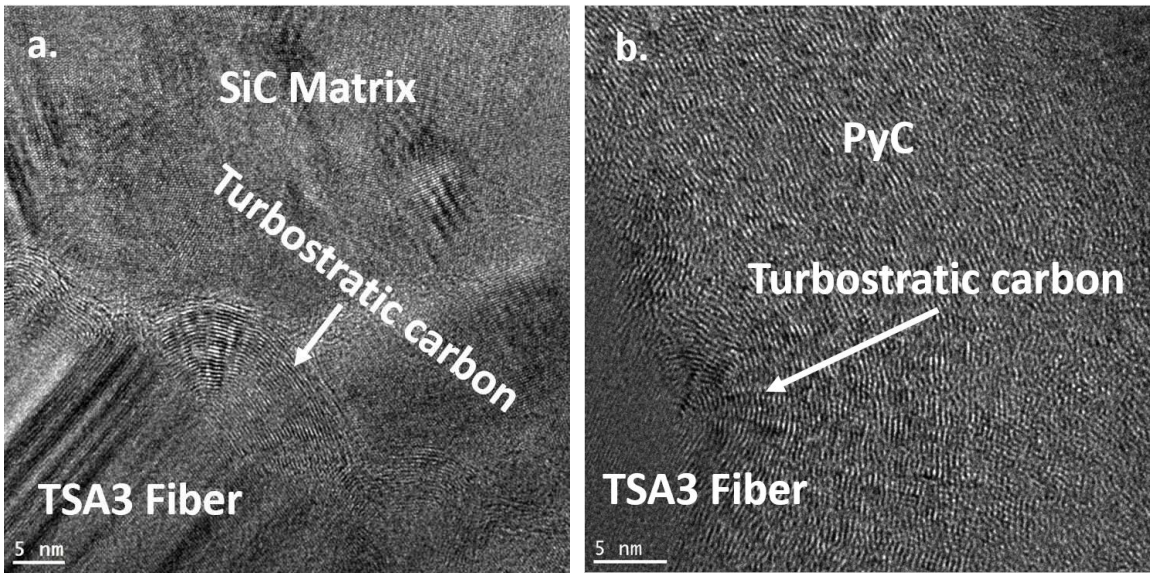

Figure 10. HRTEM image of the F/M interface of the TSA3/SiC composite (a.) and of the TSA3/PyC/SiC composite (b.)

3.3. Mechanical behavior of SiC/SiC and SiC/PyC/SiC composites

3.3.1. Tensile tests

The room temperature tensile properties of the SiC/SiC and SiC/PyC/SiC composites reinforced by HNS or TSA3 fibers are presented in table 3. The stress-strain curves of HNS/SiC and HNS/PyC/SiC composites at room temperature are shown in figure 11a. and those of TSA3/SiC and TSA3/PyC/SiC in figure 12a.

The HNS/SiC and HNS/PyC/SiC composites have equivalent Young's moduli, the PyC contribution on the total stiffness of these composites being insignificant. The HNS/PyC/SiC composites have higher failure strain and stress compared to HNS/SiC due to the PyC interphase. More surprisingly HNS/SiC composites also exhibit a pseudo-ductile mechanical behavior. Such behavior was previously attributed to the PyC interphase in HNS/PyC/SiC composites [24], [53], [54]. Thus, contrary to what was generally presupposed for CMC reinforced by SiC fibers of the 3rd generation, the deposition of an interphase is not a necessary condition for the development of micromechanisms leading to pseudoductility. The PyC interphase, however, has a positive impact on the reduction of the dipersion in the failure strains. Figures 11b. and 11c. display SEM images of the entire fracture surfaces of the HNS/SiC and HNS/PyC/SiC composites after tensile loading. Numerous HNS fibers pull-outs were observed for both composites, confirming the pseudo-ductile mechanical behavior for both HNS reinforced composites, behavior previously attributed to the PyC in HNS/PyC/SiC composites.

The failure strain of TSA3/PyC/SiC composites reached 0.22% while the TSA3/SiC one did not exceed 0.05%, corresponding to the failure strain of monolithic SiC [55]. The presence of the PyC allowed a pseudo-ductile behavior to be obtained for the TSA3/PyC/SiC composites although the failure strain and stress of TSA3/PyC/SiC composites were lower than those of the HNS/PyC/SiC composites. The dispersion of the principal mechanical characteristics was important for the TSA3/PyC/SiC composite. No fiber pull-out were observed on the fracture surfaces in the TSA3/SiC composite and pull out was limited in the TSA3/PyC/SiC composite (figures 12b. and 12c.), leading to macroscopic flat failure surfaces, which is consistent with the observed mechanical behaviour.

	E (GPa)	σ_r (MPa)	ε_r (%)
HNS/SiC	278 (± 11)	225 (±38)	0.37 (± 0.10)
HNS/PyC/SiC	268 (± 4.1)	286 (± 16.8)	0.45 (± 0.03)
TSA3/SiC	318 (± 14)	141 (± 8.7)	0.05 (± 0.02)
TSA3/PyC/SiC	315 (± 28)	275 (± 28)	0.22 (± 0.03)

Table 3. Main mechanical characteristics of HNS and TSA3 reinforced composites after tensile test: E (GPa), σ_r (MPa), ε_r (%)

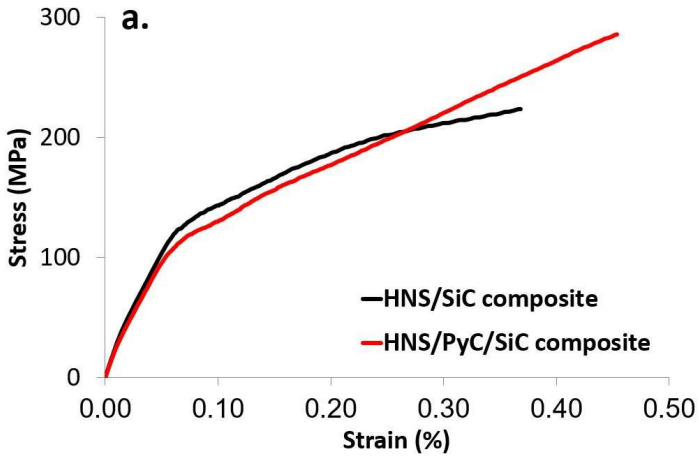

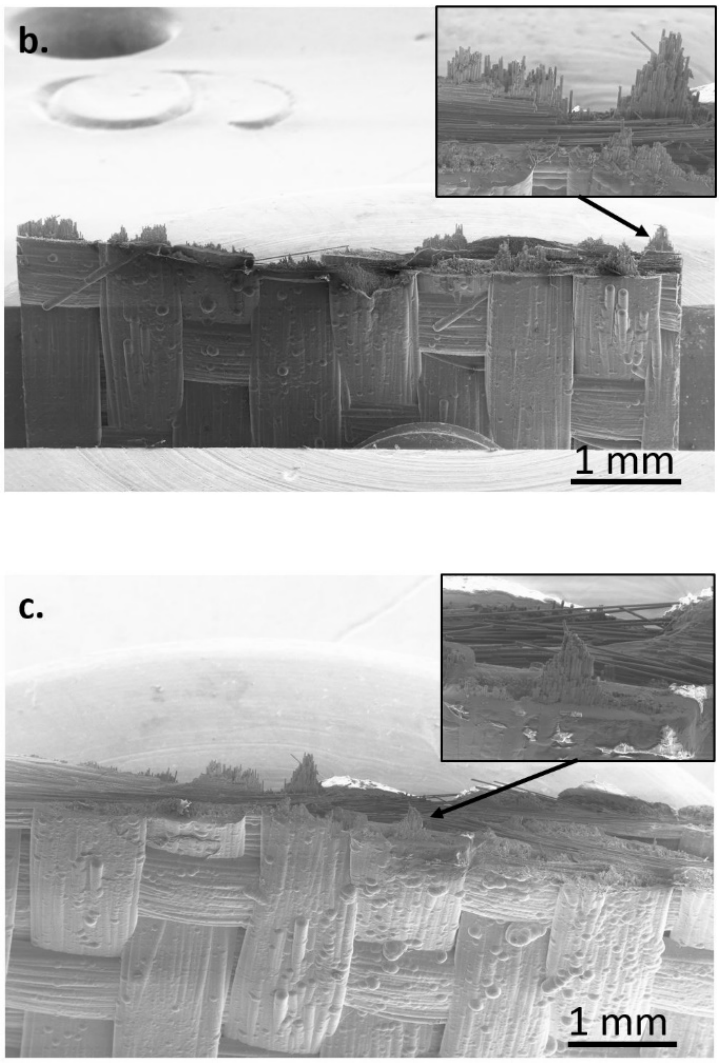

Figure 11. Tensile stress-strain curves for HNS reinforced composites (a.), fracture surfaces of HNS/SiC (b.) and HNS/PyC/SiC (c.) by SEM

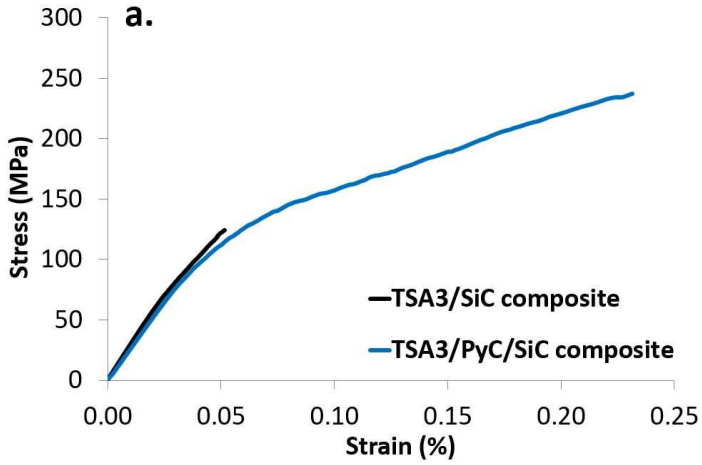

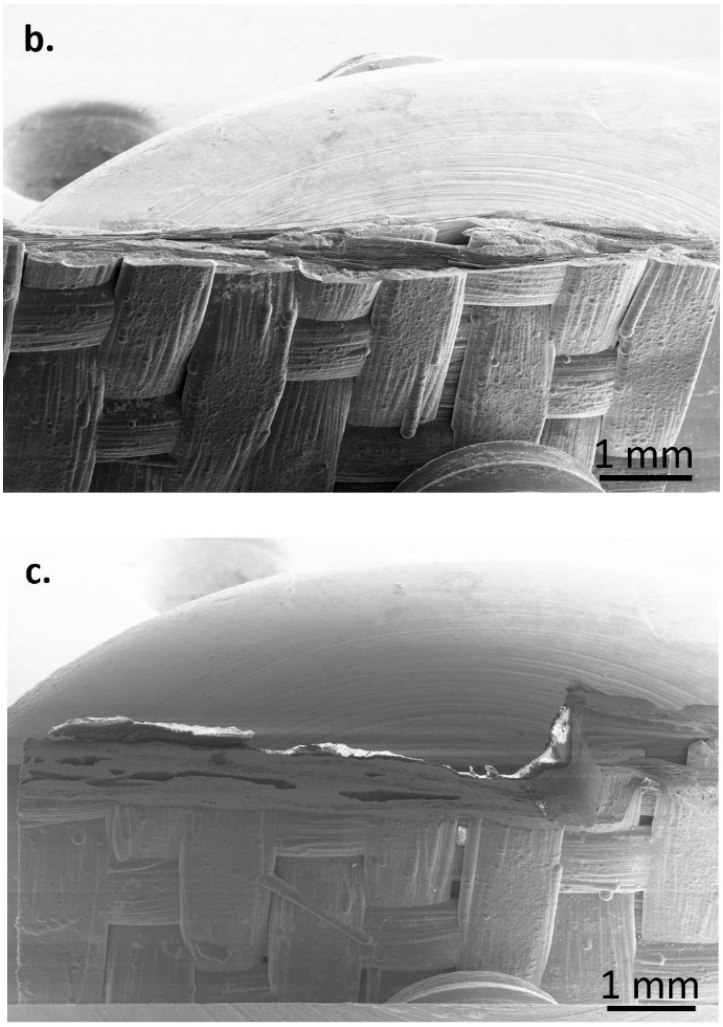

Figure 12. Tensile stress-strain curves for TSA3 reinforced composites (a.), fracture surfaces of TSA3/SiC (b.) and TSA3/PyC/SiC (c.) by SEM

3.3.2. Damage mechanisms at the F/M interface

Based on the TEM observations, a regular debonding (~ 100 nm thickness on Figure 13a.) was observed at the F/M interface of the HNS/SiC composite (without PyC). This space was filled by mounting resin during the thin foil preparation, giving rise to an uniform absorption contrast. The amorphous carbon, previously observed, is still present on the HNS fibers surface after tensile loading (Figure 13b.). Matrix cracks propagated and were deflected at the interface between the SiC matrix and the amorphous carbon layer on the SiC fibers surface, despite the absence of PyC interphase. This carbon surface layer prevented the premature fiber failures and played a major role in the interfacial coupling for the HNS/SiC composites. Within the HNS/PyC/SiC composites, debonding was also observed after tensile tests (~ 450 nm wide on Figure 13c.). This F/M debonding allowed the HNS fibers pull-out. The PyC interphase remained bounded to the SiC matrix. Matrix cracks were deflected at the amorphous carbon

/PyC interface (Figure 13d.). The amorphous carbon/PyC interface was the weakest interface of these composites and governed partially the F/M debonding.

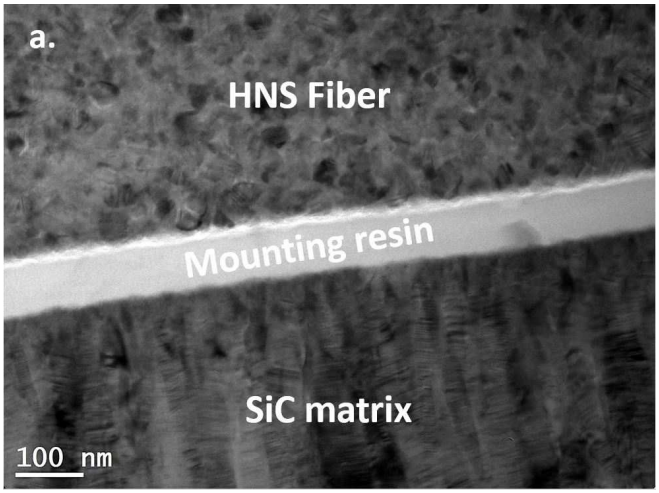

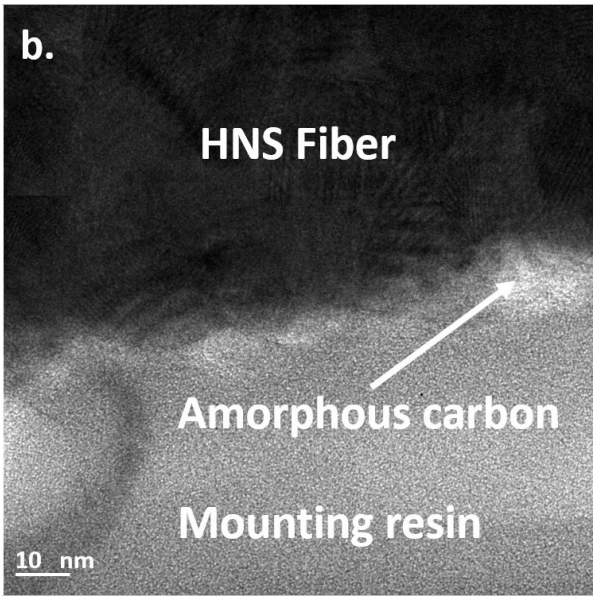

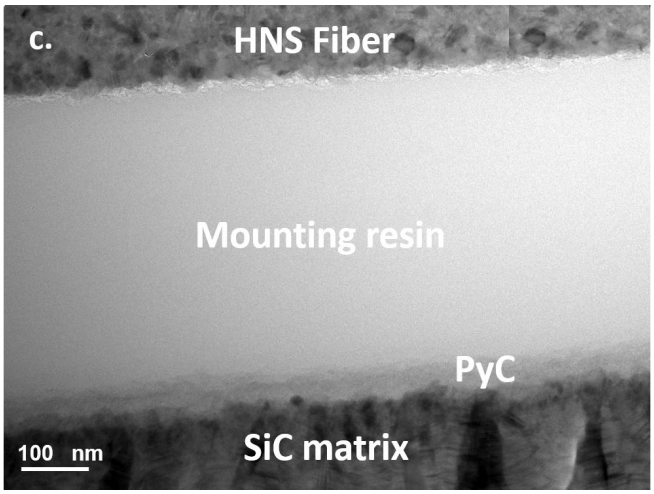

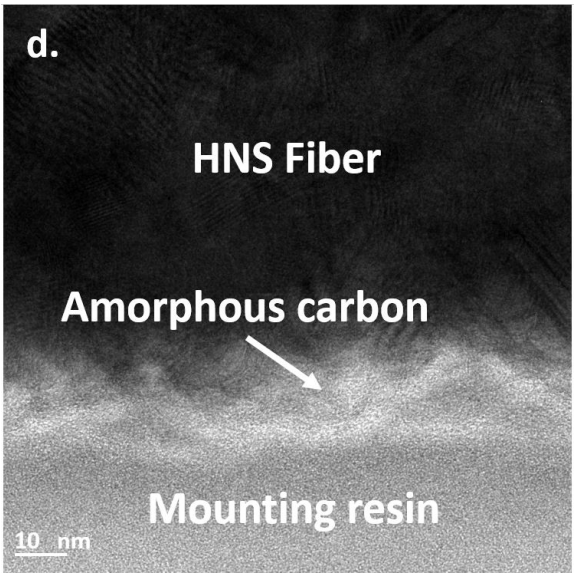

Figure 13. Damage mechanisms of HNS/SiC observed by TEM (a.) and HRTEM (b.) and damage mechanisms of HNS/PyC/SiC observed by TEM (c.) and HRTEM (d.) after tensile test

The crack opening and the F/M debonding were very limited for the TSA3-reinforced composites (Figure 14a.). Very few crack deflections were detected. The pyrocarbon interphase of TSA3/PyC/SiC composites was strongly damaged. A partial failure occurred at the PyC/C_{surf} interface but the PyC/SiC_{fiber} interface remained adhesive (Figure 14b.). On the matrix side, the PyC first stacks remained bounded to matrix SiC and were parallel to the interface. Weaker density areas within the PyC interphase were detected near the fiber surface, which were not observed prior to mechanical loading. High resolution images revealed a local reorientation of some the graphene ribbons in these areas (Figure 14c.), they might have been strongly bonded to the turbostratic carbon of the fiber surface. The interaction strength between these two carbon phases was stronger than in the case of the HNS fiber.

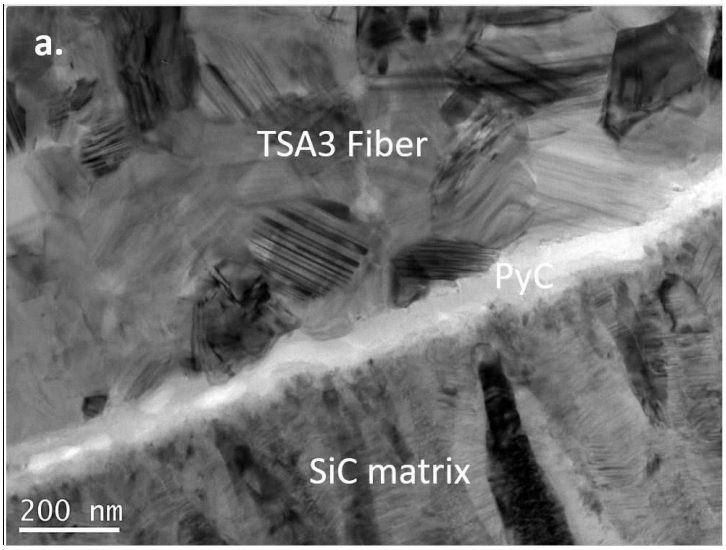

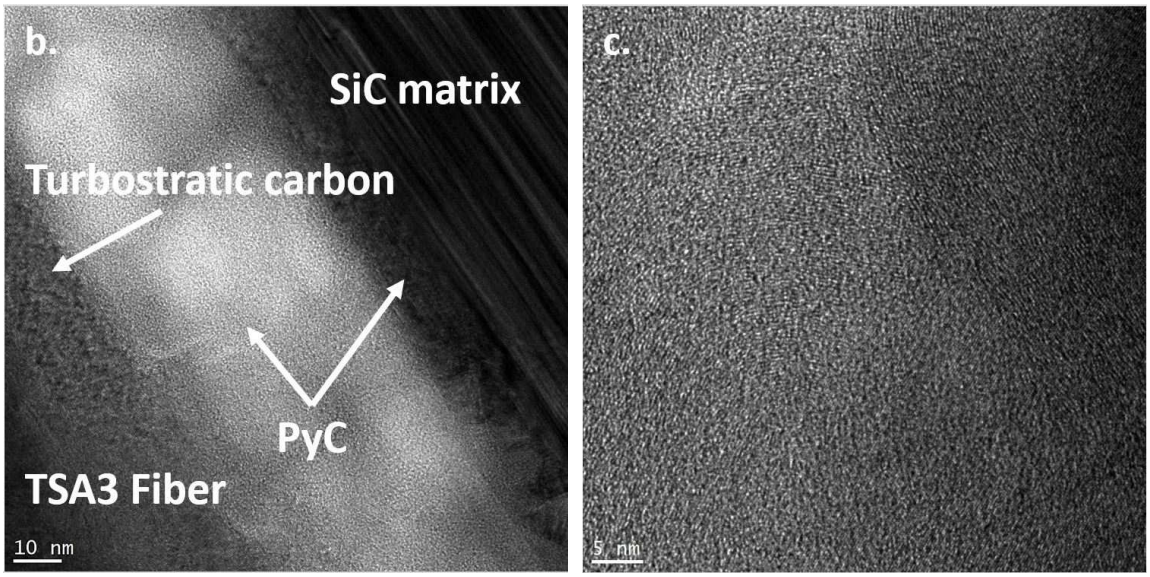

Figure 14. Damage mechanisms of TSA3/PyC/SiC observed by TEM (a.) and HRTEM (b.) after tensile test and HRTEM image of PyC interphase damage (c.)

4. Discussion

The carbon-rich extreme surfaces of the HNS and TSA3 fibers have different compositions and type of carbon bonds. These differences are not only due to the variations of fiber microstructures. The composition of their sizing polymers and their thermal decomposition mechanisms must be also considered.

Carbonaceous residues, products of PVA pyrolysis, are observed on the HNS fibers surface after desizing. A pure PVA polymer should decompose completely by heat treatment. These residues and incomplete weight loss observed during thermogravimetric analyses suggest that the chemical composition of the sizing on HNS fibers was probably not that of the pure polymer. The size disparities of these carbon residues result from heterogeneities in the thickness of the deposited PVA, linked to the sizing methodology. The HNS fiber surface is also covered by carbon layer having a similar structure than that of the carbon residues. Not being observed on HNS sized fiber surfaces, this carbon layer originates from the desizing step. The surface carbon is mainly engaged in sp^2 bonds but also for ~19 % of the atoms in sp^3 bonds. Its structure is close to that frequently observed for amorphous carbon obtained by the thermal decomposition of a polymer at high temperature and is distinct from that of the turbostratic carbon of the fiber or the PyC of the interphase.

The thermal decomposition of POE (sizing of TSA3 fibers) does not produce carbon residues on the contrary to the HNS fiber sizing. A turbostratic carbon layer is observed on the desized

TSA3 fibers surface with a majority of sp^2 hybridized C-C bonds detected by photoelectron spectroscopy. The carbon layer is not continuous leaving SiC grains uncovered on the extreme surface. This carbon rich surface is already present before the desizing and originates from the chemistry of the SiC fibers precursor. The $–CH_3$ groups of the polycarbosilane precursor are responsible for the free carbon that develops in turbostractic clusters by epitaxy on the {111} sides of the SiC grains. This turbostratic carbon is also detected on the SiC grains surface of the HNS fibers, covered by the amorphous carbon after desizing, but the pyrolysis in hydrogen atmosphere during the last step of the HNS fibers manufacturing reduces its amount. In addition the larger SiC grains size of the TSA3 fibers promotes the growth of a larger turbostratic carbon layer on their wider facets.

Two composites reinforced by HNS and TSA3 fibers were produced using the same 2.5D weaving texture and infiltration parameters of PyC interphase and SiC matrix. In the two cases the very first PyC planes are difficult to localize. For the HNS, these planes are bonded to an amorphous carbon layer covering the HNS fiber, with a possible transition toward the highly anisotropic PyC. In the TSA3 they are mainly bonded to the turbostractic carbon ribbons covering the SiC surface grains and they follow their orientations from the first PyC layers.

One of the most interesting results of this study concerns the mechanical behavior of the HNS fibers-reinforced SiC/SiC composites. The HNS/SiC and HNS/PyC/SiC composites both exhibit pseudo-ductile mechanical behavior, moderate F/M coupling and similar mechanical behavior up to a deformation of 0.2%. Fracture analysis showed that damage mode at the F/M interface is equivalent, i.e. the cracks deflection occurs on the outer surface of the amorphous carbon on the HNS fibers. Therefore, the local damage mechanisms of the HNS-reinforced composites with and without PyC interphase are governed by the bond of amorphous carbon to SiC or PyC that has a crack-deflecting function. At $\varepsilon > 0.2$ %, the damage, in HNS/PyC/SiC composites, could be reduced by the presence of PyC interphase still bounded to the matrix. The action of this interphase improved the mechanical behavior of HNS/PyC/SiC composites compared to HNS/SiC composites and limited the dispersion in the failure stresses. However, the crack deflection is firstly governed by the weaker bonds at the PyC/amorphous carbon interface that allows the interfacial debonding. The structure of the amorphous carbon, and more particularly the carbon residues of the sizing polymer (PVA), is seen to play an important role on the damage mechanisms.

The damage mechanisms of TSA3 reinforced composites differ from those of HNS reinforced ones. For the TSA3/SiC composites, fiber pull out is not possible and matrix cracks propagate

directly across TSA3 fibers leading to a fragile behavior. The presence of turbostratic carbon aggregates covering the SiC grains on TSA3 surface and the preferred orientation of the first SiC planes deposited on this carbon with $\{111\}_{SiC}//(002)_C$ during the CVI process, explain the stronger F/M coupling and the brittle behavior in TSA3/SiC composites. The PyC interphase on the TSA3 fiber increases the damage tolerance without reaching the one of the HNS/SiC or HNS/PyC/SiC composites. The damage mecanisms of TSA3/PyC/SiC composites are still difficult to explain. No net crack deflection in F/M interface is observed for these materials. The F/M bonds are very strong which mainly results in damage to the PyC interphase. The PyC has a preferred orientation on the turbostratic carbon of the TSA3 fibers surface. A reorientation and damage of PyC stacks strongly bounded to the turbostratic carbon of TSA3 fibers surface occur before the failure of these bonds. The TSA3/PyC/SiC composites can display a pseudo-ductile behavior because the PyC interface keeps its cracks deflection function and the F/M debonding is observed although with shorter pull out length than HNS/PyC/SiC or even HNS/SiC composites.

This study has revealed the major role played by a weakly organized and homogeneous carbon phase in the damage tolerance of the composites. A surface treatment of TSA3 fibers will be undertaken to obtain this amorphous carbon layer similar to that found on the HNS fibers. This layer is expected to screen the carbon turbostratic on TSA3 fibers surface, which induced strong interfacial interactions with the pyrocarbon, and to lead to an ideal F/M coupling for the TSA3/PyC/SiC composites.

5. Conclusion

We have studied the origin, the composition and the microstructure of the carbon-rich extreme surface of two SiC fibers. By understanding the chemical adhesion at the PyC/SiC fiber interface, we explain its effect on the Fiber/Matrix coupling and the resulting local damage mechanisms of SiC/SiC composites under mechanical loading. The surface characteristics of SiC fibers influence the bonding mode of the first planes of PyC interphase with the fibers, determine the intensity of the F/M coupling and the localization of the F/M debonding, control the damage mode and the macroscopic behavior.

The properties of the surface carbon are then essential and depend on the nature of the reinforcement. In one case, the desizing of HNS fibers leads to carbonaceous residues, giving

rise to an amorphous carbon layer covering completely the fibers. The TSA3 fibers surface is composed of turbostratic carbon formed during the fiber ceramisation step.

The amorphous layer, left by the thermal decomposition of PVA on HNS fibers, has a crucial role in the optimization of the mechanical behavior. Indeed, the matrix cracks are always deflected at the carbon surface.

Therefore, the weaker interface of these composites is between the carbon layer and either the PyC interphase or the SiC matrix. The damage tolerance of the composites reinforced by HNS is not only brought by the PyC interphase, but also by the amorphous carbon. The bond between amorphous carbon and PyC plays the role of the mechanical fuse whereas the pyrocarbon decrease the fiber/matrix friction.

The presence of PyC interphase is mandatory for composite reinforced by the TSA3 to bring some damage tolerance but without reaching that of HNS/PyC/SiC composite or even HNS/SiC. The strong bonding between PyC and turbostratic carbon explains this specific behaviour. We show that a weakly organized carbon layer is the key for higher damage tolerance of SiC/SiC composites and it is expected that a chemical treatment on the TSA3 would result in an improved pseudo-ductile behavior for TSA3/PyC/SiC composites.

Acknowledgements

The authors are very grateful to S. Poissonnet for the FIB preparation and scientific discussions, G. Brabant for his help in SEM images and G. Loupias for mechanical tests.

References

[1] N. P. Bansal et J. Lamon, *Ceramic Matrix Composites: Materials, Modeling and Technology*. John Wiley & Sons, 2014.

[2] F. Christin, « Design, Fabrication, and Application of Thermostructural Composites (TSC) like C/C, C/SiC, and SiC/SiC Composites », *Adv. Eng. Mater.*, vol. 4, n° 12, p. 903-912, 2002.

[3] T. Koyanagi, Y. Katoh, T. Nozawa, L.L. Snead, S. Kondo, C.H. Henager Jr., M. Ferraris, T. Hinoki, et Q. Huang, « Recent progress in the development of SiC composites for nuclear fusion applications », *J. Nucl. Mater.*, vol. 511, p. 544-555, déc. 2018.

[4] H. Ohnabe, S. Masaki, M. Onozuka, K. Miyahara, et T. Sasa, « Potential application of ceramic matrix composites to aero-engine components », *Compos. Part Appl. Sci. Manuf.*, vol. 30, nº 4, p. 489-496, avr. 1999.

[5] J. Lamon, « Chemical Vapor Infiltrated SiC/SiC Composites (CVI SiC/SiC) », in *Handbook of Ceramic Composites*, N. P. Bansal, Éd. Boston, MA: Springer US, 2005, p. 55-76.

[6] Y. Katoh, K. Ozawa, C. Shih, T. Nozawa, R. J. Shinavski, A. Hasegawa, et L.L. Snead, « Continuous SiC fiber, CVI SiC matrix composites for nuclear applications: Properties and irradiation effects », *J. Nucl. Mater.*, vol. 448, nº 1, p. 448-476, mai 2014.

[7] W. Krenkel, *Ceramic Matrix Composites: Fiber Reinforced Ceramics and Their Applications*. John Wiley & Sons, 2008.

[8] R. R. Naslain, « SiC-Matrix Composites: Nonbrittle Ceramics for Thermo-Structural Application », *Int. J. Appl. Ceram. Technol.*, vol. 2, nº 2, p. 75-84, mars 2005.

[9] Y. Katoh, T. Nozawa, L. L. Snead, K. Ozawa, et H. Tanigawa, « Stability of SiC and its composites at high neutron fluence », *J. Nucl. Mater.*, vol. 417, nº 1, p. 400-405, oct. 2011.

[10] C. P. Deck, G.M. Jacobsen, J. Sheeder, O. Gutierrez, J. Zhang, J. Stone, H.E. Khalifa, et C.A. Back, « Characterization of SiC–SiC composites for accident tolerant fuel cladding », *J. Nucl. Mater.*, vol. 466, p. 667-681, nov. 2015.

[11] R. R. Naslain, « The design of the fibre-matrix interfacial zone in ceramic matrix composites », *Compos. Part Appl. Sci. Manuf.*, vol. 29, nº 9, p. 1145-1155, janv. 1998.

[12] G. Grathwohl, A. Hähnel, B. Meier, E. Pippel, G. Richter, et J. Woltersdorf, « Fibre-reinforced SiC-matrix composites: Microstructure, interfaces and mechanical properties », *J. Eur. Ceram. Soc.*, vol. 10, nº 1, p. 1-12, janv. 1992.

[13] E. Inghels et J. Lamon, « Caractérisation de l'endommagement de composites tissés à matrice SiC », *Rev. Phys. Appliquée*, vol. 23, nº 3, p. 193-200, mars 1988.

[14] Y. Katoh, K. Ozawa, T. Hinoki, Y. Choi, L. L. Snead, et A. Hasegawa, « Mechanical properties of advanced SiC fiber composites irradiated at very high temperatures », *J. Nucl. Mater.*, vol. 417, nº 1, p. 416-420, oct. 2011.

[15] A. Oberlin, « Carbonization and graphitization », *Carbon*, vol. 22, nº 6, p. 521-541, janv. 1984.

[16] R. Naslain, « The concept of layered interphases in SiC/SiC », déc. 1995.

[17] T. Hinoki, L. L. Snead, Y. Katoh, A. Hasegawa, T. Nozawa, et A. Kohyama, « The effect of high dose/high temperature irradiation on high purity fibers and their silicon carbide composites », *J. Nucl. Mater.*, vol. 307-311, p. 1157-1162, déc. 2002.

[18] Y. Katoh, T. Nozawa, L. L. Snead, et T. Hinoki, « Effect of neutron irradiation on tensile properties of unidirectional silicon carbide composites », *J. Nucl. Mater.*, vol. 367-370, p. 774-779, août 2007.

[19] E. Buet, C. Sauder, S. Poissonnet, P. Brender, R. Gadiou, et C. Vix-Guterl, « Influence of chemical and physical properties of the last generation of silicon carbide fibres on the mechanical behaviour of SiC/SiC composite », *J. Eur. Ceram. Soc.*, vol. 32, n° 3, p. 547-557, mars 2012.

[20] C. Sauder, A. Brusson, et J. Lamon, « Mechanical Properties of Hi-NICALON S and SA3 Fiber Reinforced SiC/SiC Minicomposites », *Ceram. Eng. Sci. Proc.*, p. 89-99.

[21] A. Hasegawa, A. Kohyama, R. H. Jones, L. L. Snead, B. Riccardi, et P. Fenici, « Critical issues and current status of SiC/SiC composites for fusion », *J. Nucl. Mater.*, vol. 283-287, p. 128-137, déc. 2000.

[22] M. Y. He, A. G. Evans, et J. W. Hutchinson, « Crack deflection at an interface between dissimilar elastic materials: Role of residual stresses », *Int. J. Solids Struct.*, vol. 31, n° 24, p. 3443-3455, déc. 1994.

[23] E. Buet, « Influence des caractéristiques de surface des fibres de type Hi-Nicalon S et Tyranno SA3 sur le comportement mécanique des composites SiC/SiC », thesis, Université de Haute-Alsace, 2012.

[24] C. Sauder, A. Brusson, et J. Lamon, « Influence of Interface Characteristics on the Mechanical Properties of Hi-Nicalon type-S or Tyranno-SA3 Fiber-Reinforced SiC/SiC Minicomposites: Influence of Interface Characteristics on the Mechanical Properties », *Int. J. Appl. Ceram. Technol.*, vol. 7, n° 3, p. 291-303, févr. 2010.

[25] R. Bodet, X. Bourrat, J. Lamon, et R. Naslain, « Tensile creep behaviour of a silicon carbide-based fibre with a low oxygen content », *J. Mater. Sci.*, vol. 30, n° 3, p. 661-677, janv. 1995.

[26] J. L. Thomason et D. W. Dwight, « The use of XPS for characterisation of glass fibre coatings », *Compos. Part Appl. Sci. Manuf.*, vol. 30, n° 12, p. 1401-1413, déc. 1999.

[27] A. R. Bunsell et M.-H. Berger, « Fine diameter ceramic fibres », *J. Eur. Ceram. Soc.*, vol. 20, n° 13, p. 2249-2260, nov. 2000.

[28] S. M. Dong, G. Chollon, C. Labrugère, M. Lahaye, A. Guette, J.L. Bruneel, M. Couzi, R. Naslain, et D.L. Jiang, « Characterization of nearly stoichiometric SiC ceramic fibres », *J. Mater. Sci.*, vol. 36, n° 10, p. 2371-2381, mai 2001.

[29] C. Sauder, « Ceramic Matrix Composites: Nuclear Applications », in *Ceramic Matrix Composites*, John Wiley & Sons, Ltd, 2014, p. 609-646.

[30] H. Ichikawa, « Development of High Performance SiC Fibers Derived from Polycarbosilane Using Electron Beam Irradiation Curing-A Review », *J. Jap. Ceram. Soc.*, n° 1330, p. 455-460, 2006.

[31] W. Yang, H. Araki, A. Kohyama, J. Yu, et T. Noda, « New tyranno-SA fiber reinforced CVI-SiC/SiC composite », *J. Mater. Sci. Lett.*, vol. 21, n° 18, p. 1411-1413, sept. 2002.

[32] M. Berger et A. Bunsell, *Fine Ceramic Fibers*. CRC Press, 1999.

[33] T. Ishikawa, Y. Kohtoku, K. Kumagawa, T. Yamamura, et T. Nagasawa, « High-strength alkali-resistant sintered SiC fibre stable to 2,200 °C », *Nature*, vol. 391, n° 6669, p. 773-775, févr. 1998.

[34] E. Bouchard, J. Lavenac, J.-C. Roux, F. Langlais, et P. Delhaès, « Pyrocarbon Deposits on a Graphite Surface Observed by STM », *Chem. Vap. Depos.*, vol. 7, n° 3, p. 125-130, 2001.

[35] F. Polack, M. Silly, C. Chauvet, B. Lagarde, N. Bergeard, M. Izquierdo, O. Chubar, D. Krizmancic, M. Ribbens, J.-P. Duval, C. Basset, S. Kubsky, et F. Sirotti, « TEMPO: a New Insertion Device Beamline at SOLEIL for Time Resolved Photoelectron Spectroscopy Experiments on Solids and Interfaces », *AIP Conf. Proc.*, vol. 1234, n° 1, p. 185-188, juin 2010.

[36] A. Jablonski and C. J. Powell, "NIST Electron Inelastic-Mean-Free-Path Database", *National Institute of Standards and Technology, Gaithersburg*, 2010.

[37] L. A. Giannuzzi et F. A. Stevie, « A review of focused ion beam milling techniques for TEM specimen preparation », *Micron*, vol. 30, n° 3, p. 197-204, juin 1999.

[38] B. J. Holland et J. N. Hay, « The thermal degradation of poly(vinyl alcohol) », *Polymer*, vol. 42, n° 16, p. 6775-6783, juill. 2001.

[39] B. Rimez, H. Rahier, G. Van Assche, T. Artoos, M. Biesemans, et B. Van Mele, « The thermal degradation of poly(vinyl acetate) and poly(ethylene-co-vinyl acetate), Part I: Experimental study of the degradation mechanism », *Polym. Degrad. Stab.*, vol. 93, n° 4, p. 800-810, avr. 2008.

[40] R. T. Pogue, K. L. Ackley, et V. Majidi, « Evaluation of High Molecular Weight Species Produced during Thermal Degradation of Poly(Vinyl Alcohol) », *Int. J. Polym. Anal. Charact.*, vol. 3, n° 3, p. 193-202, mai 1997.

[41] J. B. Gilbert, J. J. Kipling, B. McEnaney, et J. N. Sherwood, « Carbonization of polymers I—Thermogravimetric analysis », *Polymer*, vol. 3, p. 1-10, janv. 1962.

[42] Y. Tsuchiya et K. Sumi, « Thermal decomposition products of polyvinyl chloride », *J. Appl. Chem.*, vol. 17, n° 12, p. 364-366, 1967.

[43] A. Choukourov, A. Grinevich, O. Polonskyi, J. Hanus, J. Kousal, D. Slavinska, et H. Biederman, « Vacuum Thermal Degradation of Poly(ethylene oxide) », *J. Phys. Chem. B*, vol. 113, n° 10, p. 2984-2984-2989, mars 2009.

[44] M. Jakić, N. S. Vrandečić, et I. Klarić, « Thermal degradation of poly(vinyl chloride)/poly(ethylene oxide) blends: Thermogravimetric analysis », *Polym. Degrad. Stab.*, vol. 98, n° 9, p. 1738-1743, sept. 2013.

[45] M. M. Fares, J. Hacaloglu, et S. Suzer, « Characterization of degradation products of polyethylene oxide by pyrolysis mass spectrometry », *Eur. Polym. J.*, vol. 30, n° 7, p. 845-850, juill. 1994.

[46] S. L. Madorsicy et S. Straus, « Thermal degradation of polyethylene oxide and polypropylene oxide », J. *Polym. Sc.*, vol. 36, n° 130, p. 183-194, 1959.

[47] A. Bianco, H.-M. Cheng, T. Enoki, Y. Gogotsi, R. H. Hurt, N. Koratkar, T. Kyotani, M. Monthioux, C. R. Park, J. M. D. Tascon, et J. Zhang, « All in the graphene family – A recommended nomenclature for two-dimensional carbon materials », *Carbon*, vol. 65, p. 1-6, déc. 2013.

[48] J. Robertson, « Amorphous carbon », *Adv. Phys.*, vol. 35, n° 4, p. 317-374, janv. 1986.

[49] J. Robertson et E. P. O'Reilly, « Electronic and atomic structure of amorphous carbon », *Phys. Rev. B*, vol. 35, n° 6, p. 2946-2957, févr. 1987.

[50] M. G. Beghi, A. C. Ferrari, K. B. K. Teo, J. Robertson, C. E. Bottani, A. Libassi, et B. K. Tanner, « Bonding and mechanical properties of ultrathin diamond-like carbon films », *Appl. Phys. Lett.*, vol. 81, n° 20, p. 3804-3806, nov. 2002.

[51] T. L. Barr et S. Seal, « Nature of the use of adventitious carbon as a binding energy standard », *J. Vac. Sci. Technol. A*, vol. 13, n° 3, p. 1239-1246, mai 1995.

[52] M. Guigon, « Relation entre la microtexture et les propriétés mécaniques et électriques des fibres de carbone ex-polyacrylo-nitrile », thesis, Compiègne, 1985.

[53] S. Bertrand, R. Pailler, et J. Lamon, « SiC/SiC minicomposites with nanoscale multilayered fibre coatings », *Compos. Sci. Technol.*, vol. 61, n° 3, p. 363-367, févr. 2001.

[54] J. Lamon, F. Rebillat, et A. G. Evans, « Microcomposite Test Procedure for Evaluating the Interface Properties of Ceramic Matrix Composites », *J. Am. Ceram. Soc.*, vol. 78, n° 2, p. 401-405, 1995.

[55] L. L. Snead, T. Nozawa, Y. Katoh, T.-S. Byun, S. Kondo, et D. A. Petti, « Handbook of SiC properties for fuel performance modeling », *J. Nucl. Mater.*, vol. 371, n° 1, p. 329-377, sept. 2007.